Theoretical maximum photogeneration efficiency and performance characterization of In$_x$Ga$_{1-x}$N/Si tandem water-splitting photoelectrodes EP

Yannick K. Gaudy, Žarko Gačević iD, and Sophia Haussener iD

COLLECTIONS

Paper published as part of the special topic on Solar to Fuel
Note: This paper is part of the Special Issue on Solar to Fuel.

EP   This paper was selected as an Editor's Pick

View Online   Export Citation   CrossMark

ARTICLES YOU MAY BE INTERESTED IN

Understanding the interplay of surface structure and work function in oxides: A case study on SrTiO$_3$
APL Materials **8**, 071110 (2020); https://doi.org/10.1063/1.5143325

Scattering mechanisms and mobility enhancement in epitaxial BaSnO$_3$ thin films probed via electrolyte gating
APL Materials **8**, 071113 (2020); https://doi.org/10.1063/5.0017227

P-block metal-based (Sn, In, Bi, Pb) electrocatalysts for selective reduction of CO$_2$ to formate
APL Materials **8**, 060901 (2020); https://doi.org/10.1063/5.0004194

Theoretical maximum photogeneration efficiency and performance characterization of In$_x$Ga$_{1-x}$N/Si tandem water-splitting photoelectrodes ᴱᴾ

Yannick K. Gaudy,[1] Žarko Gačević,[2] (ID) and Sophia Haussener[1,a] (ID)

AFFILIATIONS

[1] Institute of Mechanical Engineering, École Polytechnique Fédérale de Lausanne, 1015 Lausanne, Switzerland

[2] Instituto de Sistemas Optoelectrónicos y Microtecnología, Departamento de Ingeniería Electrónica,
Universidad Politécnica de Madrid, Ciudad Universitaria s/n, 28040 Madrid, Spain

Note: This paper is part of the Special Issue on Solar to Fuel.
[a] **Author to whom correspondence should be addressed:** sophia.haussener@epfl.ch. **Tel.:** +41 21 693 38 78

ABSTRACT

In$_x$Ga$_{1-x}$N is a promising material for flexible and efficient water-splitting photoelectrodes since the bandgap is tunable by modifying the indium content. We investigate the potential of an In$_x$Ga$_{1-x}$N/Si tandem used as a water-splitting photoelectrode. We predict a maximum theoretical photogeneration efficiency of 27% for In$_x$Ga$_{1-x}$N/Si tandem photoelectrodes by computing electromagnetic wave propagation and absorption. This maximum is obtained for an indium content between 50% and 60% (i.e., a bandgap between 1.4 eV and 1.2 eV, respectively) and a film thickness between 280 nm and 560 nm. We then experimentally assess In$_x$Ga$_{1-x}$N photoanodes with the indium content varying between 9.5% and 41.4%. A Mott–Schottky analysis indicates doping concentrations (which effectively represent defect density, given there was no intentional doping) above 8.1×10^{20} cm^{-3} (with a maximum doping concentration of 1.9×10^{22} cm^{-3} for an indium content of 9.5%) and flatband potentials between -0.33 V$_{RHE}$ for $x = 9.5\%$ and -0.06 V$_{RHE}$ for $x = 33.3\%$. Photocurrent–voltage curves of In$_x$Ga$_{1-x}$N photoanodes are measured in 1M H$_2$SO$_4$ and 1M Na$_2$SO$_4$, and the incident photon-to-current efficiency spectra in 1M Na$_2$SO$_4$. The incident photon-to-current efficiency spectra are used to computationally determine the diffusion length, the diffusion optical number, as well as surface recombination and transfer currents. A maximum diffusion length of 262 nm is obtained for an indium content of 23.5%, in part resulting from the relatively low doping concentration (9.8×10^{20} cm^{-3} at $x = 23.5\%$). Nevertheless, the relatively high surface roughness (rms of 7.2 nm) and low flatband potential (-0.1 V$_{RHE}$) at $x = 23.5\%$ cause high surface recombination and affect negatively the overall photoelectrode performance. Thus, the performance of In$_x$Ga$_{1-x}$N photoelectrodes appears to be a tradeoff between surface recombination (affected by surface roughness and flatband potential) and diffusion length (affected by doping concentration/defect density). The performance improvements of the In$_x$Ga$_{1-x}$N photoanodes are most likely achieved through modification of the doping concentration (defect density) and reduction of the surface recombination (e.g., by the deposition of a passivation layer and co-catalysts). The investigations of the ability to reach high performance by nanostructuring indicate that reasonable improvements through nanostructuring might be very challenging.

I. INTRODUCTION

In$_x$Ga$_{1-x}$N layers of high structural and optical quality grown on Si have been successfully synthesized in the last few years,[1,2] opening a new perspective for inexpensive and efficient solar harvesting devices. The theoretical maximum efficiency for such tandem photoelectrochemical (PEC) water-splitting systems could reach over 22.5%, using Si as the bottom cell and In$_x$Ga$_{1-x}$N with a bandgap between 1.6 eV and 1.8 eV[3] (corresponding to an indium content of 37%–44%, respectively[2]) as the top cell. A PEC water-splitting device utilizing concentrated irradiation and with a solar-to-hydrogen (STH) efficiency above 20% could, theoretically, lead to

a hydrogen prize below 3 \$ kg^{-1}, a prize competitive with the price of gasoline for the same amount of energy.[4,5]

Notwithstanding the high theoretical efficiency of In$_x$Ga$_{1-x}$N for solar hydrogen production, previous attempts to fabricate In$_x$Ga$_{1-x}$N water-splitting photoelectrodes have led to very poor performance with photocurrents below 0.1 mA cm^{-2} under AM1.5G irradiation, i.e., a performance even inferior to pure n-GaN with a bandgap of 3.4 eV.[6] This low performance was attributed to the low crystalline quality of In$_x$Ga$_{1-x}$N without further investigating the reasons for the gap between theoretically predicted and experimentally observed efficiencies. An in-depth investigation of In$_x$Ga$_{1-x}$N was performed based on finite element simulations of p-GaN/n-In$_x$Ga$_{1-x}$N/n-In$_{0.5}$Ga$_{0.5}$N/p-Si/n-Si solar cells, where the In$_x$Ga$_{1-x}$N layer was graded. These simulations predicted 28.9% efficiency and showed that the thickness and the doping concentration of the graded region substantially affected the performance.[7] The modeling of InGaN/Si tandem solar cells (ignoring space charge recombination) predicted a theoretical maximum efficiency of 31%.[8] These models were based on In$_x$Ga$_{1-x}$N solar cells and not on In$_x$Ga$_{1-x}$N water-splitting photoelectrodes, which are somewhat different physical systems due to the presence of the semiconductor–electrolyte interface.[9] Experimental and computational studies of In$_x$Ga$_{1-x}$N/Si tandem water-splitting photoelectrodes, to identify and quantify their main losses, are yet to be completed.

In this work, we first quantify, through theoretical evaluations of In$_x$Ga$_{1-x}$N water-splitting photoelectrodes with varying In contents, the maximum theoretical photogeneration efficiencies, before we experimentally assess their performance as photoelectrodes. We report measured photocurrent–voltage (I–V) curves and incident photon-to-current efficiencies (IPCEs) of In$_x$Ga$_{1-x}$N photoelectrodes with indium contents varying between x = 9.5% and 41.4%. The diffusion length, diffusion optical number, internal and surface losses, and a nanostructuring opportunity factor of the In$_x$Ga$_{1-x}$N water-splitting photoelectrodes were also calculated, utilizing the measured IPCE and the analytical method proposed by Gaudy and Haussener.[10] The combined computational and experimental characterization allowed us to identify main reasons for the low performance of the current In$_x$Ga$_{1-x}$N photoanodes and to suggest approaches for their improvements.

II. METHODOLOGY

A. Theoretical photogeneration efficiency of In$_x$Ga$_{1-x}$N/Si photoelectrodes

Electromagnetic waves (EMWs), propagating perpendicular to thin In$_x$Ga$_{1-x}$N layers deposited on a 350 μm thick Si substrate, give rise to interferences between the forward- and backward-propagating waves due to reflection at the In$_x$Ga$_{1-x}$N/Si interface. These interferences can lead to "wavy" generation rates inside the In$_x$Ga$_{1-x}$N semiconductor film and can be predicted by solving Maxwell's equation[11,12] (Beer–Lambert's law[13–15] or ray-tracing methods[16] are unable to properly address these effects). Thus, the generation rate and the photogeneration current density in In$_x$Ga$_{1-x}$N and Si semiconductors were calculated by solving Maxwell's curl equations for each frequency, ν,[17]

$$\nabla \times (\nabla \times \boldsymbol{E}(\boldsymbol{z}, \nu)) - k_0^2 \tilde{n}(\nu)^2 \boldsymbol{E}(\boldsymbol{z}, \nu) = 0, \tag{1}$$

where $\boldsymbol{E}(\boldsymbol{z}, \nu)$ is the local frequency-dependent electric vector field, $\tilde{n}(\nu) = n(\nu) - jk(\nu)$ is the complex refractive index, and k_0 is the free-space wavenumber. The optical power absorbed per unit volume is given by

$$P_{\text{abs}}(\boldsymbol{x}, \nu) = -\frac{1}{2} 2\pi\nu |\boldsymbol{E}(\boldsymbol{z}, \nu)|^2 \Im\{\varepsilon(\boldsymbol{x}, \nu)\}, \tag{2}$$

where $\Im\{\varepsilon(\boldsymbol{z}, \omega)\}$ is the imaginary part of the material's complex permittivity that can be calculated from the material's complex refractive index ($n + jk$) and the vacuum permittivity (ε_0): $\varepsilon = \varepsilon_r \varepsilon_0 = (n + jk)^2 \varepsilon_0$. The generation rate along the film thickness, $G(z)$, is calculated by integrating the spectral generation rate over the considered spectrum,

$$G(\boldsymbol{z}) = \int_\infty^{\nu_{\text{max}}} \frac{P_{\text{abs}}(\boldsymbol{z}, \nu)}{h\nu} d\nu, \tag{3}$$

where the upper integration boundary ν_{max} is $\nu_{\text{max}} \geq E_{\text{gap}}/h$ and h is Planck's constant. The photogeneration current, i_l, is calculated by integrating the generation rate over the thickness of the semiconductor

$$i_l = q \int_0^d G(\boldsymbol{z}) dz, \tag{4}$$

where q is the elementary charge and d is the thickness of the semiconductor.

The interface between the In$_x$Ga$_{1-x}$N and the Si layers was assumed to be perfect, and no additional interlayer (such as an electrical coupling layer) was considered. Such interlayers might in practice be required and—if well engineered—even further improve the performance.[18,19]

The EMW propagation was calculated in both the electrolyte and the semiconductors, assuming perpendicular AM1.5G front illumination (i.e., 0° incident angle) and a reflecting back boundary (refractive index for Si from Edwards[20]), as depicted in Fig. 1. The reflection loss at the semiconductor–electrolyte interface and the absorption in the electrolyte was accounted for by considering a 2 μm thick layer of water in front of the In$_x$Ga$_{1-x}$N layer (the absorption loss by the electrolyte was very small since the water extinction coefficient is below 10^{-5}, $k < 4 \times 10^{-6}$ in the visible range[21]). Indeed, the same photogenerated current density was observed using an electrolyte layer with a thickness of 100 μm or 2 μm (consistent
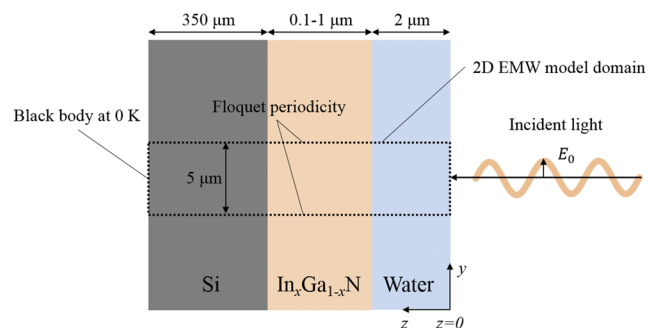

FIG. 1. Scheme of the numerical 2D EMW propagation model domain for an In$_x$Ga$_{1-x}$N/Si tandem water-splitting photoelectrode immersed in the electrolyte (not to the scale).

with absorption calculations reported in Ref. 22 or absorption effects discussed in Ref. 23), but the latter could save computational time. EMW propagation was modeled in a 2D domain (with the corresponding boundaries), enabling simulations with incident angles different from 0°. The current for an in-series tandem cell such as the $In_xGa_{1-x}N$/Si photoelectrode is limited by the lowest subcell's current. Thus, the highest photogeneration efficiency, η, of a tandem cell is obtained when the photogenerated current in all subcells is equal (i.e., subcells are current matched),

$$\eta = \min(i_{l,In_xGa_{1-x}N}, i_{l,Si})/i_0, \quad (5)$$

where $i_{l,In_xGa_{1-x}N}$ is the photogenerated current density in the $In_xGa_{1-x}N$ subcell, $i_{l,Si}$ is the photogenerated current density in the Si subcell, and i_0 is the incident photon flux at AM1.5G converted into a photocurrent density (i.e., 59.7 mA cm^{-2}). We neglected the incident UV light ($\lambda_{ph} < 400$ nm, i.e., ~10% of the incident sunlight) because the complex refractive data of $In_xGa_{1-x}N$ were available from 400 nm only[24] and because the absorption of the UV light in the electrolyte was larger than that of the visible light.[21] The subscript l is used to specify that the current is a photogenerated current and not a photocurrent (the latter also accounting for separation and injection losses). The photogeneration efficiency of $In_xGa_{1-x}N$/Si tandem photoelectrodes was investigated for varying thicknesses and indium contents (i.e., varying bandgap) of the $In_xGa_{1-x}N$ layer. The thickness of the $In_xGa_{1-x}N$ layer was varied from 10 nm to 1000 nm with the indium content varying from 17% to 59%, corresponding to an optical bandgap variation between 2.6 eV and 1.2 eV. Such bandgaps have the potential for theoretical solar-to-hydrogen (STH) efficiencies above 5% for tandem water-splitting cells.[4]

The films below 50 nm were investigated to determine if the ultrathin $In_xGa_{1-x}N$ films could benefit from resonant light trapping. Indeed, the ultrathin films of $In_xGa_{1-x}N$ would greatly reduce the amount of indium and gallium, two relatively expensive and rare materials, and reduce losses due to poor minority charge conductivity or high bulk recombination.[11] The theoretical photogeneration efficiency was also calculated without any reflection losses at the

$In_xGa_{1-x}N$/electrolyte interface and absorption in the electrolyte—by simply removing the electrolyte layer in front of the $In_xGa_{1-x}N$ film (Fig. 1)—to account for an anti-reflective coating.

The complex refractive index of $In_xGa_{1-x}N$, required in the EMW propagation model, was linearly interpolated from the data of Hazari et al.[24] The complex refractive index of $In_xGa_{1-x}N$ with varying indium contents of the photoelectrodes is depicted in Fig. 2 (samples with indium contents of $x = 9.5\%$, 16.5%, 23.5%, 33.3%, and 41.4% were used for experimental studies). The data of the complex refractive index of the single crystalline silicon layer were taken from Edwards.[20]

1. Computational details

The wavelengths used for the EMW model were varied from 400 nm to 1116 nm, corresponding, respectively, to the smallest visible wavelength and the bandgap of Si (1.11 eV i.e., 1116 nm). The ultraviolet light ($\lambda_{ph} < 400$ nm) was not considered in this work because the complex refractive index of $In_xGa_{1-x}N$ was only available between 400 nm and 1687 nm[24] and the UV light's partial absorption by the electrolyte layer.[22] The light was considered as transverse electric, and therefore, only the out-of-plane electric field was calculated. Bloch–Floquet theory was assumed for the periodicity on both sides of the computational domain (Fig. 1), which is typically used for infinite stab models where no boundary effects appear and where the phase shift is determined by a wave vector and the distance between the source and the destination.[25,26] The Maxwell's curl equations and the generation rate given by Eqs. (1)–(3) were solved with a commercial solver.[27] The convergence was obtained with a direct MUMPS solver. A relative tolerance of 10^{-4} in the electric field was used as a convergence criterion.[28] Mesh convergence was obtained for linear mesh discretization, i.e., a piecewise linear finite element basis function, with a size ratio of 4 and element numbers, n_{el}, depending on the irradiation wavelength, λ, and the layer thickness, d, namely $n_{el} = d \cdot \beta/\lambda$ with $\beta = 150$ for Si, $\beta = 200$ for $In_xGa_{1-x}N$, and $\beta = 30$ for water. The number of mesh elements perpendicular to the direction of light propagation was fixed to 5 with a width of 5 μm. We observed that for planar problems, the solver
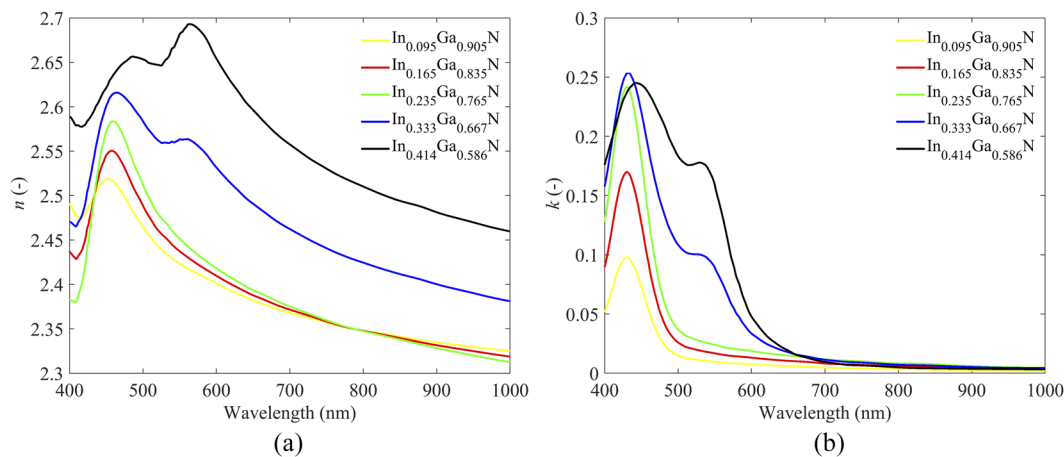

FIG. 2. (a) Real part, n, and (b) imaginary part, k, of the complex refractive index of $In_xGa_{1-x}N$ interpolated from the data of Hazari et al.[24]

was less robust using cubic or quadratic discretization orders, leading to fluctuations of the electric field in the perpendicular direction of propagation. Linear discretization needed finer meshes, but the calculation time was still reduced compared to quadratic or cubic discretization with a coarser mesh.

B. Performance and characteristics of In$_x$Ga$_{1-x}$N photoelectrodes

Experimentally, we investigated only the performance and characteristics of the In$_x$Ga$_{1-x}$N photoanodes, given that Si water-splitting photocathodes have widely been studied elsewhere.[29–34] Linear sweep voltammetry with chopped light was conducted in solutions of 1M H$_2$SO$_4$ and 1M Na$_2$SO$_3$ as a hole scavenger. The hole scavenger was used to investigate photocurrents with highly increased reaction kinetics at the In$_x$Ga$_{1-x}$N/electrolyte interface. The diffusion length, L, the diffusion optical number, $\alpha_{500}L$, the ratio of current, $R_{S,V_{IPCE}}$, the nanostructuring opportunity factor, f$_{nano}$, the surface recombination loss, the reflection loss, and the bulk loss of In$_x$Ga$_{1-x}$N photocathodes, were determined by using the method described in Ref. 10 and the corresponding in-house software POPe.[35] However, in order to fully characterize the electrode, the IPCE spectra of the photoelectrode and the following parameters are required: the complex refractive index, the bandgap, the flatband potential, the doping concentration, the relative permittivity, and the thickness of the photoelectrode. The complex refractive index of In$_x$Ga$_{1-x}$N was linearly interpolated from the data of Hazari et al.,[24] presented in Fig. 2. The bandgap of In$_x$Ga$_{1-x}$N was calculated by Vegard's law with a bowing parameter of 2.5 eV and bandgaps of 0.7 eV and 3.4 eV for InN and GaN,[2] respectively, as follows:

$$E_{\text{gap},\text{In}_x\text{Ga}_{1-x}\text{N}} = 0.7x + 3.4(1-x) - 2.5x(1-x). \quad (6)$$

The flatband potential and the doping concentration were obtained from the Mott–Schottky analysis. As our samples were not intentionally doped, our reported doping concentration represents more accurately an impurity and defect density. The equivalent circuit depicted in Fig. 6 was used to fit the measured impedance spectra. In the equivalent circuit, R$_s$ is the series resistance of the electrolyte and the semiconductor, R$_{sc}$ and C$_{sc}$ are the resistance and capacitance in the space charge region (SCR), respectively, R$_{ss}$ and C$_{ss}$ are the resistance and capacitance caused by interface states at the semiconductor–electrolyte interface, respectively. This equivalent circuit is usually used for photoelectrodes with species adsorption at the semiconductor–electrolyte interface and was previously used for n-type GaN.[36] Here, we added the Warburg diffusion element, W, an extension typically added to account for the diffusion of charges to a large planar electrode, as for In$_x$Ga$_{1-x}$N photoelectrodes[37] or as previously used for pyrite photoelectrodes.[38] Indeed, the presence of a very high doping concentration in In$_x$Ga$_{1-x}$N photoelectrodes[39] reduces the SCR to few nanometers only—below 1 nm for In$_x$Ga$_{1-x}$N (Sec. III B) at an applied potential of 1.23 V$_{RHE}$—and therefore, most of the photogenerated charges are transported by diffusion. The indium content-dependent relative permittivity of In$_x$Ga$_{1-x}$N was linearly interpolated from the relative permittivity of GaN and InN[7] as

$$\varepsilon_r(x) = 8.9(1-x) + 10.5x. \quad (7)$$

The thicknesses of the In$_x$Ga$_{1-x}$N photoelectrodes were measured by scanning electron microscopy (SEM) (Sec. II B 1).

Here, we briefly introduce the parameters obtained by the semi-analytical method of Gaudy and Haussener[10] used to characterize the performance of In$_x$Ga$_{1-x}$N photoelectrodes. The diffusion optical number is given by

$$\alpha_{500}L = \alpha(\lambda = 500 \text{ nm}) \cdot L. \quad (8)$$

The product of the absorption coefficient, α (given as $\alpha = 4\pi k/\lambda$) at a wavelength of 500 nm and the diffusion length.

Note that wave interferences were not observed in the IPCE measurements, n of InGaN for x = 9.5%–23.5% are similar to n of the GaN substrate, and therefore, the sample appears quite homogeneous and wave interferences are expected to be small, and k of InGaN was large enough to promote an exponential absorption behavior in the initial ~100 nm of the layer. For all these reasons, the exponential decrease in the generation rate seemed to be a good approximation and the procedure of Ref. 10 is applicable.

The ratio of current, given as the ratio of the surface charge transfer velocity that contributes to the water-splitting reaction, S_T, and the sum of the surface recombination velocity, S_R and S_T, is given as

$$R_{S,V_{IPCE}} = \frac{S_T}{S_T + S_R}. \quad (9)$$

The ratio of currents is given for a fixed potential, the potential at which the IPCE is measured, V_{IPCE}. For $R_{S,V_{IPCE}}$ = 1, no surface recombination occurs at the semiconductor–electrolyte interface, and for $R_{S,V_{IPCE}}$ = 0, no photocurrent is observed and electron–hole pairs fully recombine at the interface. The nanostructuring opportunity factor (which is valid only for flat photoelectrodes and not for nanostructured ones) is given by

$$\text{f}_{nano} = \log_{10}\left(\frac{\alpha_{500}L_{0.95}}{\alpha_{500}L}\right), \quad (10)$$

where $\alpha_{500}L_{0.95}$ is defined as the product of the absorption coefficient at 500 nm and the diffusion length, $L_{0.95}$ that provides internal quantum efficiency (IQE) ≥95% at 500 nm without surface recombination

$$\alpha_{500}L_{0.95} = \alpha(\lambda = 500 \text{ nm}) \cdot L_{0.95}. \quad (11)$$

A photoelectrode with f$_{nano}$ > 2 is expected not to reach high performance even when nanostructured. If f$_{nano}$ ≤ 2, it might be possible to reach higher performance when nanostructuring. If f$_{nano}$ < 0, high performance is expected even without nanostructuring. More details on these parameters can be found in our previous work.[10]

1. Experimental details

a. In$_x$Ga$_{1-x}$N photoelectrode preparation. To prepare In$_x$Ga$_{1-x}$N photoelectrodes, first, In$_x$Ga$_{1-x}$N crystalline layers with varying In contents (from 9.5% to 41.4%) and similar thicknesses (close to 500 nm) were grown on commercial KYMA templates by plasma-assisted molecular beam epitaxy.[2] The template hosts a highly n-type doped GaN layer grown on the sapphire (0006) substrate by metal–organic chemical vapor deposition (a thin insulating AlN buffer layer is deposited on the sapphire substrate, previous to the GaN growth, to improve crystal quality of the GaN epilayer grown above).
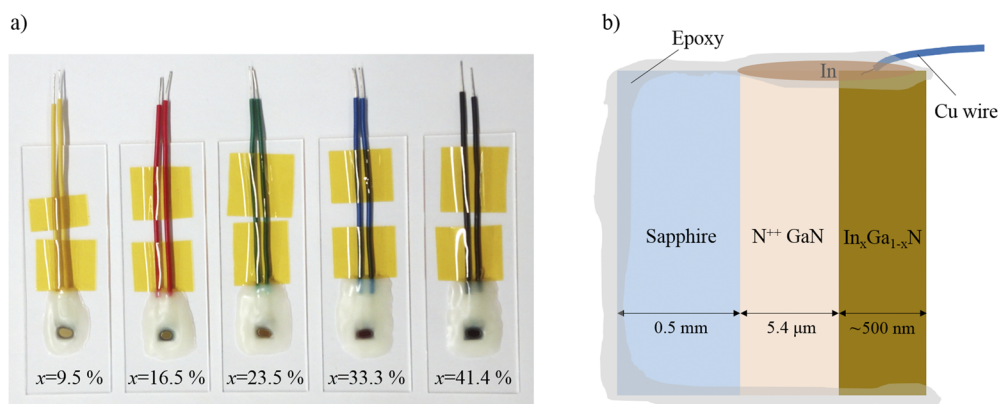
FIG. 3. (a) Image of the prepared $In_xGa_{1-x}N$ photoelectrodes. The different copper wire colors correspond to the different indium content: yellow for $x = 9.5\%$, red for $x = 16.5\%$, green for $x = 23.5\%$, blue for $x = 33.3\%$, and black for $x = 41.4\%$, as given in Table I. (b) Through-plane view schematic of the prepared photoelectrodes protected by epoxy with the ohmic contact for the electron extraction (the thin AlN buffer layer between the sapphire substrate and the highly doped GaN layer is not shown, for simplicity).

Second, the ohmic contacts were made with a scratch to put indium in contact with the highly doped GaN and the $In_xGa_{1-x}N$ layers. Third, the copper wires were fixed to indium using conductive silver paint. Finally, the photoelectrode edges and ohmic contacts were covered by white epoxy (Fig. 3). The fully exposed area for each sample is given in Table I. Typically, about 8% of the surface was covered by the epoxy (Loctite EA 9466). This epoxy is not fully opaque and (even though applied generously) transmittance in the range of ~10% in the wavelength range of interest is still possible.[40] As the diffusion length of the $In_xGa_{1-x}N$ layers was in the range of 11 nm–262 nm only (see Table III and analysis below), we believe that the inaccuracy with respect to epoxy transparency and relevant active area is negligible.

b. Characterization of the $In_xGa_{1-x}N$ layers: In content, layer thickness, surface roughness, and ohmic contact. The indium content of the $In_xGa_{1-x}N$ photoelectrodes, measured by x-ray diffraction (XRD), was found at 9.5%, 16.5%, 23.5%, 33.3%, and 41.4% (more information in the supplementary material, Fig. S1). The layer thickness was assessed by taking the average thickness of three measurements using a scanning electron microscope (supplementary material, Fig. S2). The surface topology and the surface roughness, expressed as the root mean square (rms) of the surface variation, were measured by atomic force microscopy (AFM). More details can be found in the supplementary material, Sec.

S1. The $In_xGa_{1-x}N$ photoelectrodes for the five indium contents exhibit different surface features and different surface roughnesses (see Figs. S2 and S3 in the supplementary material). Their thicknesses, on the other hand, are found similar (Table I). The ohmic contacts of the photoelectrodes were tested by measuring the resistance between two ohmic contacts separated by a distance of 3 ± 0.2 mm. The resistance was always below 16 Ω (Table I), ensuring a negligible contact resistance since the measured photocurrent was always below 0.25 mA (maximum 4 mA cm^{-2} as depicted in Fig. 5), which provides a potential shift of only 4 mV. The indium content, the layer thickness, the surface's rms, the ohmic contact resistance between two points separated by 3 ± 0.2 mm, and the surface area of all the $In_xGa_{1-x}N$ photoelectrodes are summarized in Table I.

c. PEC experimental setup and measurements. Electrochemical experiments were carried out in a three-electrode setup to refer to the potential of our measurements to the reversible hydrogen electrode. The reference electrode was Ag/AgCl (sat. KCl) and the counter electrode was Pt. The aqueous electrolyte solution was 1M H_2SO_4 and 1M Na_2SO_4. The I–V curves were obtained by using linear sweep voltammetry with a varying voltage rate of 10 mV s^{-1} in the range of 0.5 V_{RHE}–1.5 V_{RHE}. The voltage rate of 10 mV s^{-1} gave a stable steady-state current without any photocurrent hysteresis. To ensure that the $In_xGa_{1-x}N$ photoelectrodes were stable

TABLE I. Characteristics of $In_xGa_{1-x}N$ water-splitting photoelectrodes with colors as indicated in Fig. 3.

Parameters	Yellow	Red	Green	Blue	Black	Unit
Indium content, x	9.5	16.5	23.5	33.3	41.4	%
Thickness, d	532 ± 10	460 ± 5	497 ± 6	411 ± 8	509 ± 7	nm
Surface roughness, rms	4.51	5.93	7.24	12.17	11.12	nm
Ohmic contact	12	16	11	11	10	Ω
Surface area	0.086	0.0457	0.052	0.053	0.0594	cm^2

within the time of our measurements (below 5 min), chronoamperometry of the GaN photoelectrode at 1.23 V_{RHE} under AM1.5G was conducted. The photocurrent dropped only after 4 h ensuring that stability was not an issue for our measurements (Sec. S2). The electrochemical impedance spectra were measured under dark conditions in 1M H_2SO_4 at potentials varying from 0.4 to −0.6 V_{RHE} with a potential step of 50 mV and covering a frequency range between 10 Hz and 20 kHz, with ten measurements per frequency decade.

IPCE spectra were measured at 1.23 V_{RHE} from 300 nm to 900 nm in 1M Na_2SO_4 as a hole scavenger to achieve measurable photocurrents. However, the lowest wavelength used by the semi-analytical model was 420 nm because it provided better R-square values of the numerical and experimental IPCEs fitting. Indeed, the R-square was 0.5 when starting from a wavelength of 420 nm for $x = 9.5\%$ and below 0 when starting from a wavelength of 400 nm.

III. RESULTS AND DISCUSSION

A. Photogeneration efficiency of $In_xGa_{1-x}N$/Si tandem photoelectrodes

The calculated photogeneration efficiencies for varying $In_xGa_{1-x}N$ film thicknesses and bandgaps are depicted in Fig. 4 (the photogeneration efficiencies for varying $In_xGa_{1-x}N$ film thicknesses and indium contents are shown in the supplementary material, Fig. S6a). The theoretical maximum efficiency of 27% is slightly lower than the previous prediction of 31% for InGaN/Si solar cells.[8] The photogenerated current density at the maximum efficiency of 27% is 16.8 mA cm^{-2} (compared to 59.7 mA cm^{-2} at 100%). Two regions with maximum efficiency can be observed: a region with a lower bandgap 1.2 eV–1.4 eV (indium content of 59%–51%) and a lower film thickness 300 nm–550 nm, and a region

FIG. 4. Film thickness and bandgap-dependent photogeneration efficiency of $In_xGa_{1-x}N$/Si tandem water-splitting photoelectrodes with an electrolyte layer. The Si bottom layer is fixed at a thickness of 350 μm and the irradiation has an incidence angle of 0°.

with a higher bandgap ≈1.5 eV ($x = 47\%$) and a higher film thickness 700 nm–900 nm. The lower bandgap region corresponds to a photogeneration efficiency limited by the photogenerated current in the Si subcell. Namely, a top cell bandgap of 1.2 eV–1.4 eV can absorb most of the light, thus, its thickness must be reduced to let enough light reach the bottom Si subcell. By contrast, the efficiency of the 1.5 eV bandgap region is limited by the $In_xGa_{1-x}N$ subcell, and therefore, its thickness must be increased up to 700 nm to enhance the photogenerated current in the $In_xGa_{1-x}N$ subcell itself.

As can be seen from our calculations, the maximum theoretical efficiency can only be obtained for $In_xGa_{1-x}N$ bandgaps between 1.2 eV and 1.5 eV, that is, slightly lower than the computationally predicted ideal and optimum photoelectrochemical full tandem device with 1.6 eV–1.8 eV bandgap top subcell (in the case of the $In_xGa_{1-x}N$ film, it corresponds to an indium content of 37%–44%) and the Si bottom subcell.[3] The maximum photogeneration efficiency of $In_xGa_{1-x}N$ bandgaps between 1.6 eV and 1.8 eV would reach up to 23.5% with a bandgap of 1.6 eV and a thickness of 1 μm. Reducing the thickness will reduce the efficiency to 6% at a bandgap of 1.8 eV and a thickness of 100 nm.

The photogeneration efficiency, considering a perfect antireflective coating without any reflection loss at the $In_xGa_{1-x}N$/electrolyte interface and no electrolyte absorption, is depicted in Fig. S6c. The electrolyte absorption is negligible for our 100 μm water layer. However, the absence of the air–electrolyte and electrolyte–$In_xGa_{1-x}N$ interfaces omits the overall reflectance losses in the electrolyte layer of 12%. The maximum efficiency, therefore, increases to 31% (~3% more than the efficiency including the reflection losses) and a current density of 18.7 mA cm^{-2}. In addition, in that case, two maximum efficiency regions can be observed, a first region with low bandgaps between 1.2 eV and 1.4 eV and low film thicknesses of 300 nm–550 nm, and a second region with a bandgap of 1.5 eV and film thicknesses between 700 nm and 900 nm.

If the water or electrolyte layer absorption was more significant (i.e., the layer was thicker), the peak efficiency would be further reduced. Additionally, since the water absorption is more significant for larger wavelengths, the bottom cell (the Si cell) would be more significantly affected by the water absorption and the location of the second photogeneration peak (limited by the Si cell, see Fig. 4) would be shifted, requiring a thinner $In_xGa_{1-x}N$ layer and a smaller In content (or larger bandgap).

The generation rates of the ultrathin $In_xGa_{1-x}N$ film on the Si film showed clear interference between forward- and backward-propagating waves (Fig. S7) but no resonant light trapping (Fig. S8). Indeed, resonant light trapping occurs for the ultrathin film deposited on a highly reflective material, such as gold or silver.[11,12] The real part of the refractive index of Si is $n = 3.55$–5.59 for visible light and does not yet lead to resonant light trapping (i.e., the reflectivity is still relatively small), in contrast to gold with $n = 0.04$–0.09 or silver with $n = 0.1$–1.67 (both leading to significantly higher reflectivity).

The obtained photogeneration rates, together with bandgap information, can already be used in detailed balance limits and electrochemical load models[3,41] to give initial indications if the possible open circuit potential will suffice (i.e., is at least few 100 mV larger than the equilibrium potential of the reaction).
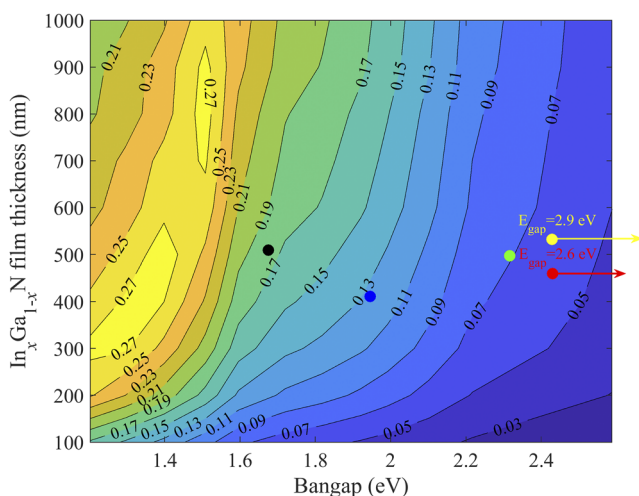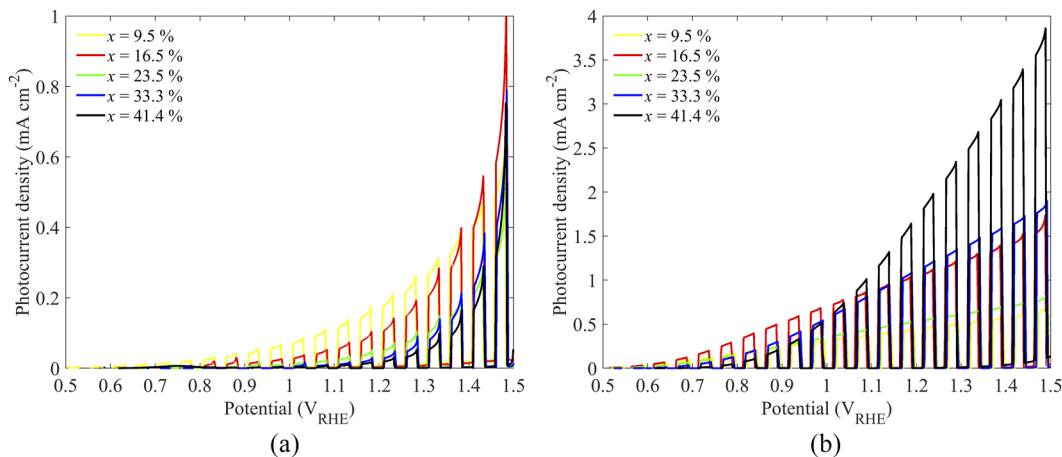
FIG. 5. Photocurrent–voltage curves of $In_xGa_{1-x}N$ photoelectrodes with chopped light in (a) 1M H_2SO_4 and (b) 1M Na_2SO_4.

B. Performance characteristics of $In_xGa_{1-x}N$ photoelectrodes

1. I–V curves of $In_xGa_{1-x}N$ photoanodes

The I–V curves of $In_xGa_{1-x}N$ photoanodes with chopped light in 1M H_2SO_4 and 1M Na_2SO_4 are depicted in Fig. 5. The fact that the photocurrent density at 1.23 V_{RHE} 1M H_2SO_4 decreases with an increase in the indium content is in conflict with the generated charge carriers, the density of which increases with an increase in the indium content [since the bandgap decreases, Fig. 5(a)], indicating that light absorption is not the dominant mechanism to limit efficiency. The photocurrent density at 1.23 V_{RHE} in 1M Na_2SO_4 [Fig. 5(b)] does not decrease with the indium content but neither does it follow a continuous increase. Indeed, the photocurrent density increases from $x = 9.5\%$ to 16.5%, then decreases at $x = 23.5\%$ and then increases again, reaching the maximum photocurrent density of 1.9 mA cm^{-2} at $x = 41.4\%$. The photocurrent dropped from 1.1 mA cm^{-2} to 0.6 mA cm^{-2} (at 1.23 V_{RHE}) with the In content increasing from 16.5% to 23.5%, while the doping concentration decreased from 1.4×10^{22} cm^{-3} to 9.8×10^{20} cm^{-3} (Fig. 6 and Table II). These results were unexpected, as a lower doping concentration (or defect density) usually leads to a reduction of the bulk[42] and surface[43] recombinations, as well as a higher minority charge mobility[44] and a larger SCR width, all factors that should positively affect the photocurrent[45] (see Fig. S12).

The decrease of the photocurrent in 1M H_2SO_4 with an increase in the indium content and the irregular variation of the photocurrent depending on the indium content in 1M Na_2SO_4 appeared to be correlated with the surface roughness (expressed in root mean square, rms) of the photoelectrode. The rms of the surface roughness of our $In_xGa_{1-x}N$ films increased continuously with the indium content (expected for $x = 41.4\%$, where it stagnated), as depicted in Table I. Thus, we hypothesize that the photocurrent decrease in 1M H_2SO_4 electrolyte is caused by dominant surface recombination resulting from the increased surface roughness (see Fig. S12). The situation is different when using a hole scavenger, since the surface recombination is decreased by the enhanced charge transfer kinetics (thus,

the surface roughness' effect on surface recombination is reduced). Nevertheless, a weak correlation between the surface roughness and the photocurrent at 1.23 V_{RHE} in the case of operation with a hole scavenger is still observed: rms at $x = 23.5\%$ is 7.2 nm and depicts stronger surface features (see the supplementary material, Fig. S3) than at $x = 16.5\%$ with an rms of 5.9 nm, accompanied by a photocurrent drop when increasing x from 16.5% to 23.5% [Fig. 5(b)]; when the In content is increased from 33.3% to 41.4%, the rms is slightly reduced (from 12.2 nm to 11.1 nm), while the photocurrent is doubled [Fig. 5(b)]. More detailed investigations supporting our hypothesis are presented in the next sections based on the doping concentration, the flatband potential, the diffusion length, the diffusion optical number, and the ratio of currents.

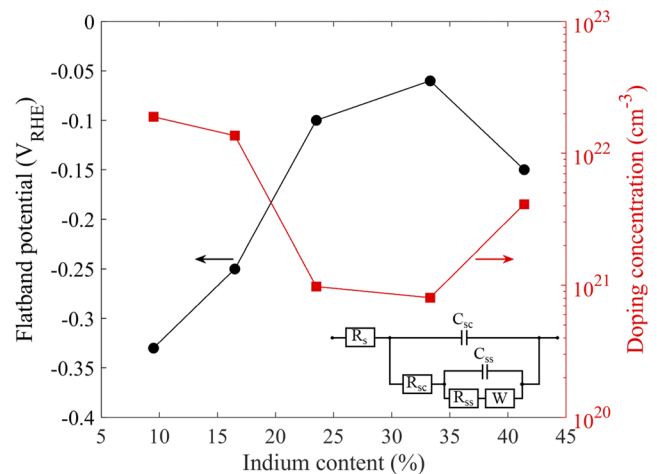**FIG. 6**. Flatband potential (left y-axis) and doping concentration (right y-axis) of $In_xGa_{1-x}N$ water-splitting photoelectrodes determined by the Mott–Schottky analysis (Fig. S10 in the supplementary material). The equivalent circuit for the electrochemical impedance spectrum fit is also indicated.

TABLE II. Numerical values of the material parameters of $In_xGa_{1-x}N$ water-splitting photoelectrodes used to determine the parameters of Table III.[10,35]

Parameters	$x = 9.5\%$	$x = 16.5\%$	$x = 23.5\%$	$x = 33.3\%$	$x = 41.4\%$	Unit
Relative permittivity, ε_r	9.1	9.2	9.3	9.4	9.6	
Bandgap, E_{gap}	2.9	2.6	2.3	1.9	1.7	eV
Flatband potential, V_{FB}	−0.33	−0.25	−0.1	−0.06	−0.15	V_{RHE}
Donor concentration, N_D^+	1.9×10^{22}	1.4×10^{22}	9.8×10^{20}	8.1×10^{20}	4.1×10^{21}	cm^{-3}
Wavelength range	420–460	420–477	400–539	400–653	400–729	

The rather strong (and nearly linear) increase in the photocurrent with an increase in the potential (potentials beyond 1.23 V vs RHE) seems to indicate that—at least for the samples that have low surface recombination (see the ratio of the current in Sec. III B 3 and the IPCE simulations in Fig. S11)—the bulk recombination dominates their performance. The reasons why for such cases the current keeps increasing is not fully resolved.

Note that we utilize 1.23 V vs RHE for the comparison and later for the IPCE measurements as it allows for large enough photocurrents that the measurements are more accurate while avoiding the range in which the dark current exponentially increases.

2. Flatband and doping concentration of $In_xGa_{1-x}N$ photoanodes

The flatband potential and the doping concentration for varying indium contents are depicted in Fig. 6. More details on the Mott–Schottky analysis can be found in the supplementary material (Sec. S4). The largest flatband potential is −0.33 V_{RHE} and is obtained at $x = 9.5\%$, while the smallest flatband potential is −0.06 V_{RHE} for $x = 33.3\%$. The doping concentrations (or defect density) are very high for all our samples and In contents and range between 8.1×10^{20} cm^{-3} ($x = 33.3\%$) and 1.9×10^{22} cm^{-3} ($x = 9.5\%$). The high doping concentration (or defect density) of $In_xGa_{1-x}N$ is probably the main cause for the low efficiency of these photoelectrodes. As previously mentioned, a high doping concentration causes a reduction in the minority charge mobility[44] and an increase in the bulk[42] and surface recombinations.[43] Moreover, the SCR width being below 1 nm at a doping concentration $\geq 8.1 \times 10^{20}$ cm^{-3}, the charge carrier separation is driven by diffusion and not drift, which further reduces the performance of the photoelectrodes. Thus, we estimate that lowering the doping concentration (or defect density) could be a fast approach for increasing the efficiency of $In_xGa_{1-x}N$ photoelectrodes. Lowering the doping concentration could also prolong the charge carriers' lifetime, as observed for GaN.[46]

3. Diffusion length, diffusion optical number, ratio of currents, and nanostructuring opportunity factor

Table II (the layer's thickness is given in Table I) summarizes the different material parameters required to determine the diffusion length, the diffusion optical number, the ratio of currents, and the nanostructuring opportunity factor [Sec. II B, Eqs. (8)–(11)].[10] The calculated performance parameters of $In_xGa_{1-x}N$ photoelectrodes are given in Table III. The highest diffusion length, 262 nm, is

obtained for $x = 23.5\%$, then for $x = 33.3\%$ with a diffusion length of 158 nm, 32 nm for $x = 9.5\%$, 16 nm for $x = 41.4\%$, and 11 nm for $x = 16.5\%$. The diffusion length correlates with the doping concentration (or defect density), as expected. For $x = 23.5\%$ and $x = 33.3\%$, the diffusion lengths are above 100 nm, while the doping concentrations are below 10^{21} cm^{-3}, whereas for $x = 9.5\%$, 16.5%, and 41.4% the diffusion lengths are below 100 nm and the doping concentrations are above 10^{21} cm^{-3}. Thus, the higher the doping concentration, the lower the diffusion length.

The diffusion optical number and the ratio of transfer to total currents are key parameters to understand the performance of $In_xGa_{1-x}N$ photoelectrodes. The diffusion optical number is maximized at $x = 23.5\%$, in accordance with the diffusion length (Table III) and the lower doping concentration (Fig. 6). However, the flatband potential is smaller (−0.1 V_{RHE} for $x = 23.5\%$ compared to −0.25 V_{RHE} for $x = 16.5\%$), which reduces the space charge region potential, and thus, increases surface recombination. Moreover, the surface roughness is also increased (rms = 5.9 nm for $x = 23.5\%$ to rms = 7.2 nm for $x = 23.5\%$), which can further increase the surface recombination. The combined negative effects of the lower flatband potential and the higher surface roughness are reflected in the ratio of current that is significantly decreased from $R_{S,V_{IPCE}} = 0.96$ at $x = 16.5\%$ to $R_{S,V_{IPCE}} = 0.07$ at $x = 23.5\%$. In other words, the surface recombination loss is significantly increased from $x = 16.5\%$ to $x = 23.5\%$ (see Fig. S11). The experimental and numerically predicted IPCE spectra of all $In_xGa_{1-x}N$ photoelectrodes are featured in Fig. S11, together with the numerically predicted internal, reflection, and surface recombination losses.

The increase in the surface recombination loss appears to be uncompensated by the increase in the diffusion optical number. Thus, the overall performance is reduced when the In content is

TABLE III. Calculated diffusion length, L, diffusion optical number, $\alpha_{500}L$, nanostructuring opportunity factor, f_{nano}, and ratio of currents, $R_{S,V_{IPCE}}$, of $In_xGa_{1-x}N$ photoelectrodes.

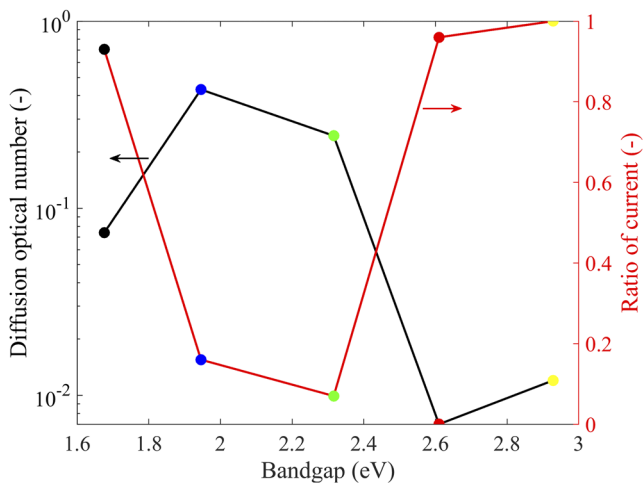| Parameters	$x = 9.5\%$	$x = 16.5\%$	$x = 23.5\%$	$x = 33.3\%$	$x = 41.4\%$
L (nm)	32	11	262	158	16
$\alpha_{500}L$	0.012	0.007	0.244	0.431	0.074
$R_{S,V_{IPCE}}$	1	0.96	0.07	0.16	0.93
f_{nano}	3.2	3.4	1.9	1.6	2.4

FIG. 7. Diffusion optical number (left y-axis) and the ratio of transfer to total current (right y-axis) of In$_x$Ga$_{1-x}$N photoelectrodes as functions of the bandgap (or indium content). The dot colors correspond to the indium content according to Table II and Fig. 3.

increased from $x = 16.5\%$ to $x = 23.5\%$, as observed by the photocurrent drop depicted in Fig. 5(b), even if the photogeneration current and the diffusion length are increased. It appears that the hole scavenger (Na$_2$SO$_4$) is unable to fully suppress the surface recombination. In our opinion, the combined effect of the surface roughness and high doping concentration (or defect density) gives rise to fast surface recombination kinetics that competes with the hole scavenger oxidation reaction kinetics (see Fig. S12).

Aside of the special case of In$_x$Ga$_{1-x}$N photoelectrodes with $x = 23.5\%$ and $x = 33.3\%$ with higher diffusion optical number and lower ratio of currents (Fig. 7), the photocurrent in 1M Na$_2$SO$_4$ increases with an increase in the In content [i.e., decreasing bandgap, Fig. 5(b)]. Indeed, the photocurrent increases from $E_{gap} = 2.9$ eV ($x = 9.5\%$) to $E_{gap} = 2.6$ eV ($x = 16.5\%$), and from $E_{gap} = 1.9$ eV ($x = 33.3\%$) to $E_{gap} = 1.7$ eV ($x = 41.4\%$).

Finally, the nanostructuring opportunity factors, f$_{nano}$, of In$_x$Ga$_{1-x}$N photoelectrodes were predicted, indicating that only In$_x$Ga$_{1-x}$N photoelectrodes at $x = 23.5\%$ and $x = 33.3\%$ show some performance improvement potential through nanostructuring. As f$_{nano}$ remains only slightly lower than 2 (1.6 for $x = 33.3\%$ and 1.9 for $x = 23.5\%$), performance improvements are expected to be more successful through reducing the doping concentration (or defect density) rather than working on nanostructuring.

IV. CONCLUSION

Tunable bandgap photoelectrode materials can be a route to highly efficient and inexpensive PEC water-splitting devices. We calculated a theoretical maximum efficiency of 27% for In$_x$Ga$_{1-x}$N/Si tandem photoelectrodes for an indium content between 50% and 60% (bandgap between 1.2 eV and 1.4 eV) and a film thickness between 280 nm and 560 nm. A maximum efficiency of 31%

was obtained when neglecting surface reflection losses (i.e., by neglecting the electrolyte and incorporating an anti-reflecting coating). Despite the high theoretical efficiency of In$_x$Ga$_{1-x}$N/Si tandem photoelectrodes, our fabricated In$_x$Ga$_{1-x}$N photoelectrodes (with an indium content varying from 9.5% to 41.4%) led to a maximum photocurrent density of only 1.9 mA cm^{-2} at 1.23 V$_{RHE}$ for $x = 41.4\%$ and when using a hole scavenger (1M Na$_2$SO$_4$) electrolyte. This photocurrent density represents only 8% of the maximum theoretical photocurrent density of 23.8 mA cm^{-2} for a semiconductor with a bandgap of 1.7 eV (corresponding to In$_x$Ga$_{1-x}$N with $x = 41.4\%$). We observed that the surface roughness, the flatband potential, and the doping concentration played key roles in the performance of In$_x$Ga$_{1-x}$N photoanodes. As the samples were not intentionally doped, the doping concentration represents more precisely an impurity and defect density. The diffusion length and the electron/hole generation are higher for $x = 23.5\%$ (bandgap of 2.3 eV and diffusion length of 262 nm), but the photocurrent density in 1M Na$_2$SO$_4$ was smaller for $x = 23.5\%$ than that for $x = 16.5\%$ (bandgap of 2.6 eV and diffusion length of 11 nm). Indeed, the higher surface roughness and the lower flatband potential for $x = 23.5\%$ are causing a higher surface recombination loss and an overall lower photocurrent compared to the $x = 16.5\%$ case. Aside of the In$_x$Ga$_{1-x}$N photoelectrodes with $x = 23.5\%$ and $x = 33.3\%$ that showed not only higher surface recombination loss but also higher diffusion length (thanks to their relative lower doping concentration or defect density), the performance of In$_x$Ga$_{1-x}$N photoelectrodes in 1M Na$_2$SO$_4$ was mainly driven by the bandgap, i.e., the lower the bandgap, the more light is absorbed and converted to electron/hole pairs, leading to the higher performance. In 1M H$_2$SO$_4$, the performance of In$_x$Ga$_{1-x}$N photoelectrodes is limited by the surface recombination that is extremely high and hinders comparison between the photoelectrodes of different indium contents. Our Mott–Schottky analysis showed that the doping concentration or defect density for In$_x$Ga$_{1-x}$N photoelectrodes was extremely high, i.e., a doping concentration higher than 8.1×10^{20} cm^{-3} for all indium contents (Table II) were measured. Thus, we mostly attribute the low performance of In$_x$Ga$_{1-x}$N photoanodes to their high doping concentration (or defect density).

We estimated that nanostructuring could improve the performance of these photoanodes, especially In$_x$Ga$_{1-x}$N photoanodes with $x = 23.5\%$ and $x = 33.3\%$ (Table III). However, efforts on reducing the doping and defect concentration should be prioritized to increase the efficiency of In$_x$Ga$_{1-x}$N photoanodes. Indeed, the doping concentration of 4.1×10^{21} cm^{-3} for $x = 41.4\%$ leads to a diffusion length of only 16 nm and a diffusion optical number of 0.074. A reduction in doping concentration and defect density might be achieved by optimizing the molecular beam epitaxy growth of In$_x$Ga$_{1-x}$N layers, or by using an alternative synthesis method. Generally, we believe that research progress in the III–V photovoltaics community in recent years might be translated also to such photoelectrodes, especially with respect to reduction of surface recombination and broadly the electrode–electrolyte interface engineering.

We showed that the combined usage of an analytical IPCE model[10] and common experimental methods, such as SEM images, AFM surface topography, experimental IPCE, and the Mott–Schottky analysis, appears to be a powerful way to investigate the

performance of $In_xGa_{1-x}N$ photoanodes and is general so that it can be applied to any emerging photoelectrode materials.

SUPPLEMENTARY MATERIAL

See the supplementary material for details on the sample growth and In-content quantification, SEM and surface roughness measurements, photocorrosion measurements, photogeneration calculations, the Mott–Schottky analysis, IPCE measurements and calculations, and an overview plot of In-content on performance and correlations between relevant parameters.

ACKNOWLEDGMENTS

DATA AVAILABILITY

The data that support the findings of this study are available from the corresponding author upon reasonable request.

REFERENCES

[1]P. Aseev et al., "Near-infrared emitting In-rich InGaN layers grown directly on Si: Towards the whole composition range," Appl. Phys. Lett. **106**, 072102 (2015).

[2]P. Aseev et al., "Uniform low-to-high in composition InGaN layers grown on Si," Appl. Phys. Express **6**, 115503 (2013).

[3]S. Haussener, S. Hu, C. Xiang, A. Z. Weber, and N. S. Lewis, "Simulations of the irradiation and temperature dependence of the efficiency of tandem photoelectrochemical water-splitting systems," Energy Environ. Sci. **6**(12), 3605–3618 (2013).

[4]B. A. Pinaud et al., "Technical and economic feasibility of centralized facilities for solar hydrogen production via photocatalysis and photoelectrochemistry," Energy Environ. Sci. **6**(7), 1983 (2013).

[5]M. Dumortier, S. Tembhurne, and S. Haussener, "Holistic design guidelines for solar hydrogen production by photo-electrochemical routes," Energy Environ. Sci. **8**(12), 3614–3628 (2015).

[6]J. Juodkazytė et al., "$In_xGa_{1-x}N$ performance as a band-gap-tunable photoelectrode in acidic and basic solutions," Sol. Energy Mater. Sol. Cells **130**, 36–41 (2014).

[7]G. F. Brown, J. W. Ager, W. Walukiewicz, and J. Wu, "Finite element simulations of compositionally graded InGaN solar cells," Sol. Energy Mater. Sol. Cells **94**(3), 478–483 (2010).

[8]L. Hsu and W. Walukiewicz, "Modeling of InGaN/Si tandem solar cells," J. Appl. Phys. **104**(2), 024507 (2008).

[9]A. J. Nozik and R. Memming, "Physical chemistry of semiconductor–liquid interfaces," J. Phys. Chem. **100**(31), 13061–13078 (1996).

[10]Y. K. Gaudy and S. Haussener, "Rapid performance optimization method for photoelectrodes," J. Phys. Chem. C **123**, 21838–21851 (2019).

[11]H. Dotan et al., "Resonant light trapping in ultrathin films for water splitting," Nat. Mater. **12**(11), 158–164 (2013).

[12]S. Suter, R. Graf, D. Moreno García, and S. Haussener, "Optimizing and implementing light trapping in thin-film, mesostructured photoanodes," ACS Appl. Mater. Interfaces **12**(5), 5739–5749 (2020).

[13]A. Berger and J. Newman, "An integrated 1-dimensional model of a photoelectrochemical cell for water splitting," J. Electrochem. Soc. **161**(8), E3328–E3340 (2014).

[14]P. Cendula et al., "Calculation of the energy band diagram of a photoelectrochemical water splitting cell," J. Phys. Chem. C **118**, 29599–29607 (2014).

[15]T. J. Mills, F. Lin, and S. W. Boettcher, "Theory and simulations of electrocatalyst-coated semiconductor electrodes for solar water splitting," Phys. Rev. Lett. **112**(14), 148304 (2014).

[16]R. Siegel and J. Howell, Thermal Radiation Heat Transfer, 4th ed. (Taylor & Francis, New York, 2002).

[17]D. M. Pozar, Microwave Engineering, 4th ed. (Wiley, 2012).

[18]Y. Piekner et al., "Implementing strong interference in ultrathin film top absorbers for tandem solar cells," ACS Photonics **5**(12), 5068–5078 (2018).

[19]X. Shi et al., "Unassisted photoelectrochemical water splitting exceeding 7% solar-to-hydrogen conversion efficiency using photon recycling," Nat. Commun. **7**(1), 11943 (2016).

[20]D. F. Edwards, "Silicon (Si)∗," in Handbook of Optical Constants of Solids, edited by E. D. Palik (Academic Press, 1985), Vol. I, pp. 547–569.

[21]G. M. Hale and M. R. Querry, "Optical constants of water in the 200-nm to 200-μm wavelength region," Appl. Opt. **12**(3), 555–563 (1973).

[22]H. Döscher, J. F. Geisz, T. G. Deutsch, and J. A. Turner, "Sunlight absorption in water – efficiency and design implications for photoelectrochemical devices," Energy Environ. Sci. **7**(9), 2951–2956 (2014).

[23]B. Parkinson, "On the efficiency and stability of photoelectrochemical devices," Acc. Chem. Res. **17**(12), 431–437 (1984).

[24]A. Hazari et al., "Optical constant of $In_xGa_{1-x}N$ ($0 \le x \le 0.73$) in the visible and near-infrared wavelength regimes," Opt. Lett. **40**(14), 3304–3307 (2015).

[25]A. Nicolet, S. Guenneau, C. Geuzaine, and F. Zolla, "Modelling of electromagnetic waves in periodic media with finite elements," J. Comput. Appl. Math. **168**, 321–329 (2004).

[26]E. A. B. Cole, Mathematical and Numerical Modelling of Heterostructure Semiconductor Devices: From Theory to Programming (Springer, 2009).

[27]Comsol Inc., Comsol Multiphysics, 2016.

[28]Y. K. Gaudy and S. Haussener, "Utilizing modeling, experiments, and statistics for the analysis of water-splitting photoelectrodes," J. Mater. Chem. A **4**(8), 3100–3114 (2016).

[29]Y. Hou et al., "Bioinspired molecular co-catalysts bonded to a silicon photocathode for solar hydrogen evolution," Nat. Mater. **10**(6), 434–438 (2011).

[30]S. Li et al., "Enhanced photoelectrochemical performance of planar p-silicon by APCVD deposition of surface mesoporous hematite coating," Appl. Catal., B **200**, 372–377 (2017).

[31]X. Li et al., "Photoelectrochemical hydrogen evolution of tapered silicon nanowires," Phys. Chem. Chem. Phys. **17**(2), 800–804 (2015).

[32]F. Urbain, V. Smirnov, J.-P. Becker, and F. Finger, "Impact of light-induced degradation on the performance of multijunction thin-film silicon-based photoelectrochemical water-splitting devices," ACS Omega **1**(5), 832–836 (2016).

[33]C. Xiang, A. C. Meng, and N. S. Lewis, "Evaluation and optimization of mass transport of redox species in silicon microwire-array photoelectrodes," Proc. Natl. Acad. Sci. U. S. A. **109**(39), 15622–15627 (2012).

[34]A. Goossens, E. M. Kelder, R. J. M. Beeren, C. J. G. Bartels, and J. Schoonman, "Structural, optical, and electronic properties of silicon/boron phosphide heterojunction photoelectrodes," Ber. Bundesforschungsanst. Phys. Chem. **95**, 503–510 (1991).

[35]Y. K. Gaudy, POPe v.1.: Performance Optimization of Photoelectrode, EPFL, 2019.

[36]M. Ono et al., "Photoelectrochemical reaction and H_2 generation at zero bias optimized by carrier concentration of n-type GaN," J. Chem. Phys. **126**(5), 054708 (2007).

[37] A. J. Fujii and L. R. Faulkner, *Electrochemcical Methods: Fundamentals and Application*, 2nd ed. (John Wiley & Sons, Inc., 2001).

[38] S. Lehner, M. Ciobanu, K. Savage, and D. E. Cliffel, "Electrochemical impedance spectroscopy of synthetic pyrite doped with As, Co, and Ni," J. Electrochem. Soc. **155**(5), P61–P70 (2008).

[39] B. S. Yadav, P. Mohanta, R. S. Srinivasa, and S. S. Major, "Electrical and optical properties of transparent conducting $In_xGa_{1-x}N$ alloy films deposited by reactive co-sputtering of GaAs and indium," Thin Solid Films **555**, 179–184 (2014).

[40] H. Döscher, J. L. Young, J. F. Geisz, J. A. Turner, and T. G. Deutsch, "Solar-to-hydrogen efficiency: Shining light on photoelectrochemical device performance," Energy Environ. Sci. **9**(1), 74–80 (2016).

[41] K. T. Fountaine, H. J. Lewerenz, and H. A. Atwater, "Efficiency limits for photoelectrochemical water-splitting," Nat. Commun. **7**, 13706 (2016).

[42] E. Gaubas and J. Vanhellemont, "Comparative study of carrier lifetime dependence on dopant concentration in silicon and germanium," J. Electrochem. Soc. **154**(3), H231 (2007).

[43] A. Cuevas, P. A. Basore, G. Giroult-Matlakowski, and C. Dubois, "Surface recombination velocity of highly doped n-type silicon," J. Appl. Phys. **80**(6), 3370–3375 (1996).

[44] T. T. Mnatsakanov, M. E. Levinshtein, L. I. Pomortseva, S. N. Yurkov, G. S. Simin, and M. A. Khan, "Carrier mobility model for GaN," Solid-State Electron. **47**(1), 111–115 (2003).

[45] S. M. Sze and K. K. Ng, *Physics of Semiconductor Devices*, 3rd ed. (John Wiley & Sons, Inc., Hoboken, 2007).

[46] H. Kumano *et al.*, "Effect of indium doping on the transient optical properties of GaN films," Appl. Phys. Lett. **75**(19), 2879–2881 (1999).